Journal of Materials Science: Materials in Electronics
https://doi.org/10.1007/s10854-018-8789-6

Boosting the electrochemical capacitive properties of polypyrrole using carboxylated graphene oxide as a new dopant

Haihan Zhou[1] · **Hua-Jin Zhai**[1]

Received: 12 December 2017 / Accepted: 17 February 2018

Abstract

We report a new dopant, carboxylated graphene oxide (GO–COOH), to boost the electrochemical capacitive properties of polypyrrole (PPy). Herein, PPy/GO–COOH composite electrodes are fabricated via a facile one-pot electrochemical polymerization in aqueous dispersion containing pyrrole monomers and GO–COOH, in which GO–COOH is obtained from GO through treatment with carboxylation. Electrochemical measurements indicate that PPy/GO–COOH composite electrodes possess markedly enhanced electrochemical capacitive properties as compared to PPy/GO composite electrodes. It is because that the GO–COOH, all-round carboxyl-covered nanosheets with edged and basal oxygen-containing sites, provides more active sites for PPy heterogeneous nucleation. In contrast, the nanosheets of GO only use the edged carboxyl groups. The as-prepared PPy/GO–COOH composite electrodes exhibit electrochemical capacitive properties with a high areal specific capacitance of 170.9 mF cm^{-2} at 0.5 mA cm^{-2}, superior rate capability, as well as cycling stability (retaining 96.9% of initial capacitance for 5000 cycles). This work is anticipated to stimulate further research interest for GO–COOH based composite electrodes in electrochemical energy storage applications.

1 Introduction

The growing demands for energy-storage devices with high-power density have motivated extensive researches in supercapacitors in recent years. Compared to batteries and fuel cells, supercapacitors typically have remarkably longer cycle life, as well as superior capacity for rapid charge and discharge [1–4]. Currently, growth of flexible and portable electronic devices has been stimulating the urgent and rapid development of supercapacitors. However, great challenges still exist in order to obtain high-performance supercapacitors, owing to their relatively low energy density [5].

Supercapacitors can be classified into electrical double-layer capacitors (EDLCs) and pseudocapacitors on the basis of charge-storage mechanism. EDLCs store energy by accumulating charges at electrode/electrolyte interface, which commonly employ carbonaceous materials with high surface area. For pseudocapacitors, energy is stored by fast and reversible Faradaic redox reactions that occur at the surface and/or in the bulk of electroactive materials, usually using transition metal oxides or conducting polymers (CPs) as electrode materials [6–8]. Currently, considerable research efforts have focused on exploring novel electrode materials, particularly composite electrode materials that can combine the advantages of both EDLCs and pseudocapacitor, improving the energy density of supercapacitors, and simultaneously keeping their high power density and high cyclability [9–17].

Polypyrrole (PPy), one kind of conducting polymers, has been extensively investigated as electrode materials for supercapacitors, because it exhibits advantages such as high electrical conductivity, large storage capacity, low cost, and environmental stability. However, swelling and shrinkage would take place during charging–discharging process due to the doping/dedoping of counter anions, consequently resulting in poor cycle life [18, 19]. Another drawback of PPy is its dense growth, showing a compact morphology, which restricts the access of electrolyte to interior sites of the polymer and thus leads to dissatisfactory capacitive behaviors [20]. To improve the supercapacitive performances of PPy,

---

✉ Haihan Zhou
hhzhou@sxu.edu.cn

✉ Hua-Jin Zhai
hj.zhai@sxu.edu.cn

[1] Institute of Molecular Science, Key Laboratory of Materials for Energy Conversion and Storage of Shanxi Province, Key Laboratory of Chemical Biology and Molecular Engineering of Education Ministry, Shanxi University, Taiyuan 030006, China

a number of PPy composites have been developed lately, such as PPy/Co$(OH)_2$ [21], PPy/MnO_2 [22],PPy/Ag [23], PPy/carbon quantum dots [24], and PPy/carbon nanotube [25, 26] composites.

Graphene oxide (GO) is a monolayer sheet of graphite oxide, whose basal planes and edges are abundant with various oxygenous groups, such as hydroxyl, epoxide, carbonyl, and carboxyl. It has become a common starting material for graphene-based applications because GO sheets can be produced in large quantities [27]. The tunable oxygen-containing functional groups of GO contribute to the modification of the surface, making it a promising material to form composites with other materials. Thereinto, PPy/GO composite based supercapacitors have attracted great interest due to their considerable capacitive performances [28–34]. In these studies, although GO is insulating (1.28×10^{-9} S cm^{-1} of electrical conductivity), PPy/GO composites still show acceptable electrical conductivity around 10 S cm^{-1}, which is probably caused by the π–π stacking between GO layers and pyrrole rings. Furthermore, the introduced GO sheets provide extra mechanical support and allow room for the volume swelling and shrinkage of PPy, consequently leading to better long-term cycling stability. Besides, the hydrophilic GO will increase the wettability of composite electrodes and improve their electrochemical performances in aqueous electrolytes.

PPy/GO composites have been synthesized via either chemical or electrochemical oxidation of pyrrole monomers in the presence of GO. For chemical synthesis, the composites prepared often require being mixed with binders and additives to construct electrode. In contrast, electropolymerization is carried out by directly growing electroactive substance on the current collector, enabling easy and one-step preparation. For one-step electrochemical codeposition of PPy/GO composite electrodes, the relatively large anionic GO as a weak electrolyte is entrapped in the PPy composites, as well as serves as an effective charge-balancing dopant within the PPy matrix. Thereinto, the anionic nature of GO mainly originates from ionization of carboxyl groups on it. In particular, carboxyl groups on the surface of GO nanosheets act as active sites for PPy nucleation during polymerization [29]. However, GO sheets have quantities of hydroxyl and epoxy groups bound on the basal planes, in addition to lesser carboxyl groups located at the edges [35]. Therefore, the prepared PPy/GO composites only utilize the edged carboxyl groups to bond PPy, leaving the ample basal oxygenated groups intact, which means polymerized PPy aggregates at the edges of GO rather than being dispersed on the basal planes, as shown in Fig. 1. More importantly, the deficiency of GO as counter anion, due to limited number of carboxyl groups only at the edges, will result in lesser PPy being incorporated into the composites, restricting the enhancement of electrochemical capacitive properties.

According to the above analysis, it is believed that making sufficient use of quantities of hydroxyl and epoxy groups on the basal planes of GO sheets represents a promising route toward improving supercapacitive performances of PPy/GO composites. For this purpose, we propose in this work to convert hydroxyl and epoxy groups on the basal planes of GO sheets to carboxyl groups through carboxylation

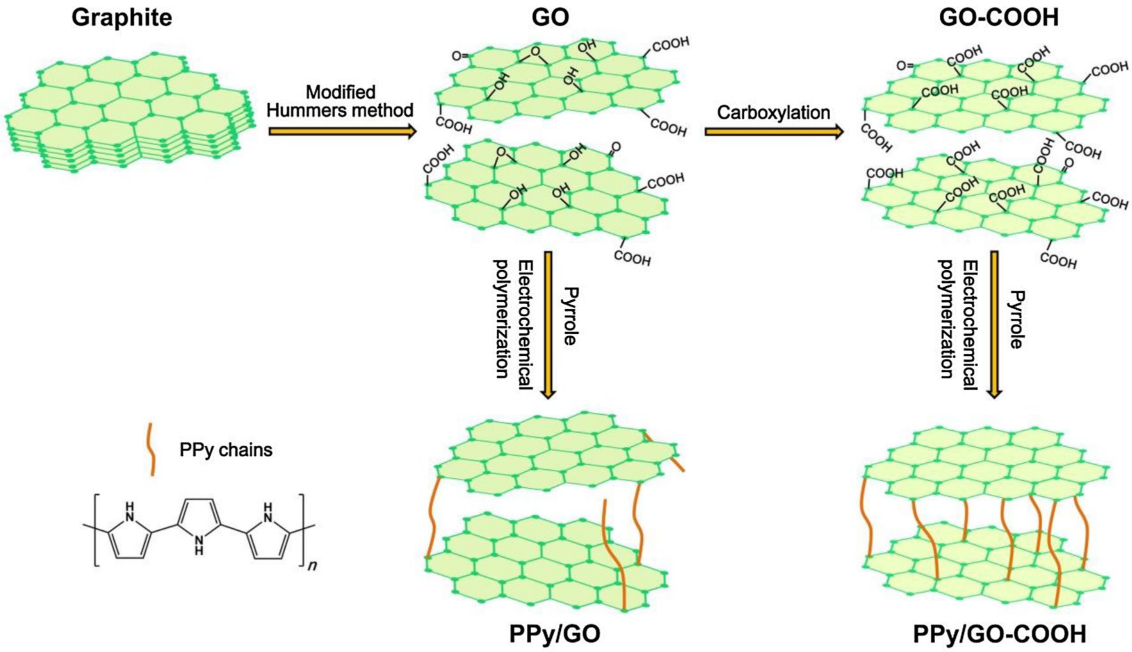

Fig. 1 Schematic illustration of the preparation processes of GO, GO–COOH, PPy/GO, and PPy/GO–COOH

treatment. Subsequently we can fabricate the carboxylated GO (GO–COOH). All-round carboxyl-covered nanosheets with edged and basal oxygen-containing sites will provide more active sites for PPy heterogeneous nucleation, which also facilitates the formation of a stable, uniform, orderly composite structure.

Herein, PPy/GO–COOH and PPy/GO composites were prepared by a facile one-pot electrochemical codeposition in aqueous dispersion containing pyrrole monomers and GO–COOH and GO, respectively. As expected, the obtained PPy/GO–COOH composite electrodes show different morphology and improved electrochemical capacitive properties as compared to PPy/GO composite electrodes. With superior electrochemical capacitive properties of high specific capacitance, good rate capability, and long-term cycling stability, the PPy/GO–COOH composite electrodes are promising for applications in energy storage.

2 Experimental

2.1 Electrode preparations

As illustrated in Fig. 1, GO was prepared from graphite powder according to a modified Hummers method [36, 37]. Carboxylation of GO was performed based on the procedure reported previously [38]. In brief, GO–COOH was obtained from GO through reacting with chloroacetic acid (Cl–CH_2–COOH) under strong alkaline condition to convert the hydroxyl (–OH) and epoxide (C–O–C) into carboxylic acid (COOH) moieties. In our investigation, 6.0 g of NaOH and 5.0 g of chloroacetic acid were added to 50 mL of GO aqueous suspension (2.0 mg mL^{-1}) and reacted under bath-sonication for 3 h. The resulting GO–COOH suspension was neutralized, filtered, and washed several times with deionized water (DW) to remove the excess reactant and dried at 50 °C in vacuum oven for 24 h.

Both PPy/GO–COOH and PPy/GO electrodes were fabricated by one-step electrochemical co-deposition. For PPy/GO–COOH electrodes, the aqueous bath for electrodeposition, composed of 0.2 M pyrrole monomer and 2 mg mL^{-1} GO–COOH, was dispersed adequately under ultrasonication before use. Graphite papers with 1×1 cm of conductive areas serve as the substrate, a Pt foil with large area acts as the counter electrode, and a saturated calomel electrode (SCE) as the reference electrode. Electrodeposition was performed in the three-electrode system with a constant low current density of 1 mA cm^{-2} for 30 min. After that, the obtained PPy/GO–COOH electrodes were rinsed with DW to remove monomer and oligomer residues. For comparison, PPy/GO electrodes were prepared with the same procedure in an aqueous deposition bath containing 0.2 M pyrrole monomer and 2 mg mL^{-1} GO. Likewise, PPy electrodes were obtained in an aqueous deposition bath consisting of 0.2 M pyrrole monomer and 0.01 M poly(styrene sulfonate) as counter anion.

2.2 Characterizations

Water contact angle was determined by Krüss DSA 100 drop shape analyzer. UV–Vis absorption spectra were recorded with Hitachi U-3900 spectrophotometer using quartz cuvette with 1 cm optical path. X-ray photoelectron spectroscopy (XPS) was recorded with Thermo ESCALAB 250 X-ray photoelectron spectrometer. Fourier transform infrared (FT-IR) spectroscopy was performed using Bruker Tensor 27 FT-IR spectrometer. X-ray diffraction (XRD) was carried out by Rigaku Ultima IV X-ray diffractometer. The morphology of samples was observed using a field emission scan electron microscope (FE-SEM, JSM-6701F, JEOL) and a high-resolution transmission electron microscopy (HRTEM, Tecnai G2 F20, FEI). Energy dispersive X-ray spectroscopy (EDS) was measured using a SEM (S-4800, Hitachi) equipped with an X-ray energy dispersive spectrometer. For FT-IR, XRD, and TEM characterizations, the samples were scraped from the deposit coated conducting glasses, because it would scrape off graphite when scraping from the surface of the deposit coated graphite papers.

2.3 Electrochemical measurements

Electrochemical capacitive performances of electrodes were tested by a two-electrode system, which consisted of two pieces of identical as-prepared electrodes. A filter paper soaked with 1.0 M KCl aqueous solution, acting as the separator, was sandwiched in between the two pieces of electrodes. The CV, GCD, and EIS data were recorded using a Chenhua CHI660E electrochemical workstation. The EIS plots were acquired at a frequency range from 10^5 to 10^{-2} Hz with a 5 mV (rms) AC sinusoid signal relative to the open circuit potential.

3 Results and discussion

3.1 Material characterizations

Figure 2a shows a homogenous brown-yellow GO and a black GO–COOH colloidal dispersion in DW, respectively. Compared with DW, both dispersions exhibit a distinct Tyndall effect, which indicates the colloidal behavior of GO and GO–COOH, facilitating the preparation of GO or GO–COOH composites with PPy through electrochemical polymerization in the homogenous colloidal deposition bath. Figure 2b shows the water contact angle of GO and GO–COOH. We can see that GO–COOH (40.7°) has smaller

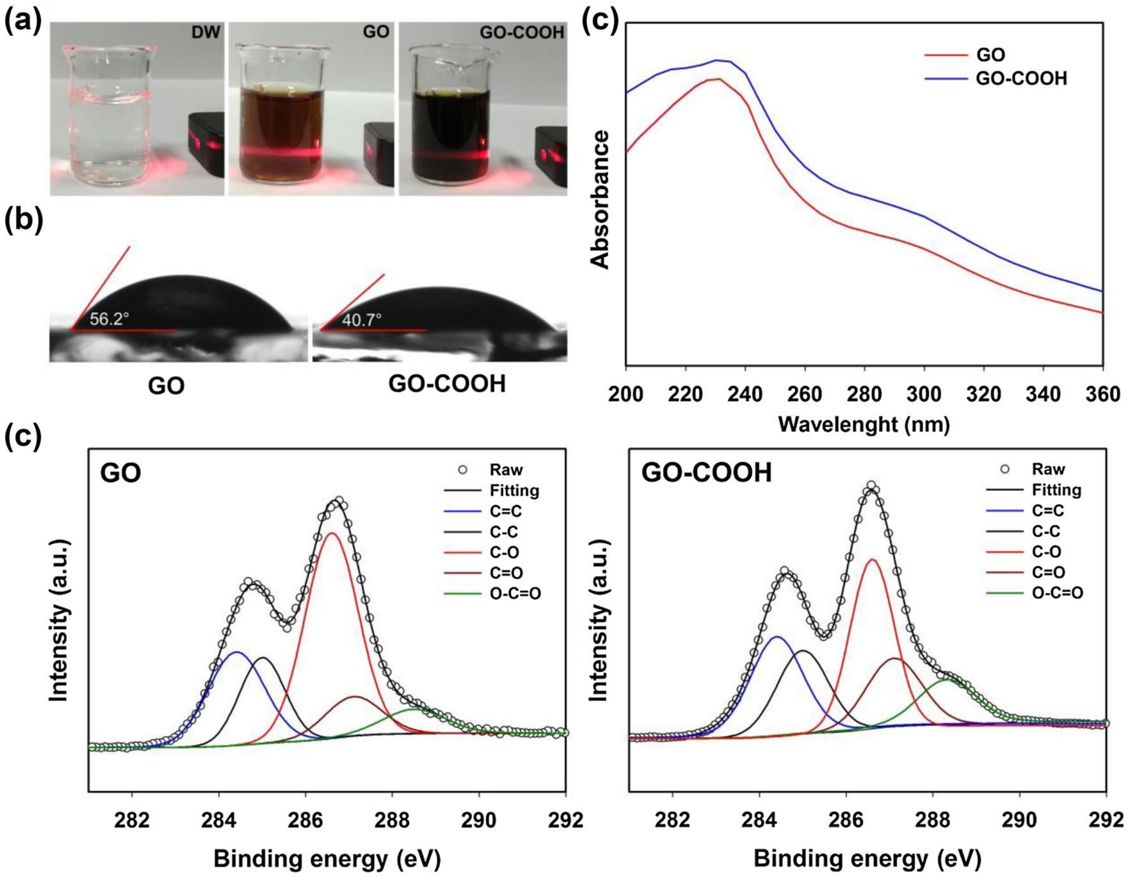

Fig. 2 **a** The Tyndall scattering effect of 1 mg mL^{-1} of GO and GO–COOH in deionized water (DW); **b** Water contact angle measurements of GO and GO–COOH films spread evenly on glasses; **c** Uv–Vis spectra of 0.01 mg mL^{-1} GO and GO–COOH in aqueous solution; **d** C 1 s XPS spectra of GO and GO–COOH

contact angle than GO (56.2°), indicative of better hydrophilicity for GO–COOH, which is favourable for the access of electrolyte. Figure 2c shows UV–vis spectra of GO and GO–COOH. Both GO and GO–COOH have a strong characteristic peak at around 230 nm that corresponds to π–π^* transition of aromatic C–C bonds, as well as a shoulder peak at 300 nm originated from n-π^* transition of C=O bonds [39]. In addition, the increase in absorbance led to color change from brown-yellow for GO to black for GO–COOH; see Fig. 2a. This color change can be ascribed to the restoration of electronic conjugation within the graphene plane, which is possibly related to the opening of epoxide rings and hydrolysis of esters on GO under alkaline conditions during the carboxylation process [40].

High-resolution C 1s XPS spectra of GO and GO–COOH are presented in Fig. 2d. Both spectra are deconvoluted into five fitting peaks, located at 284.4, 285, 286.6, 287.1, and 288.5 eV, which originate from C=C bonds formed by sp^2 carbon, C–C bonds formed by sp^3 carbon, C–O, C=O, and O–C=O, respectively. Furthermore, it can be calculated based on the peak area that the proportion of C–O in various C species for GO and GO–COOH decreases from 43.6 to 29.2%, while the proportion of O–C=O increases from 8.5 to 14.0%. This implies that the hydroxyl (–OH) and epoxide (C–O–C) on the basal plane of GO are partially converted into carboxylic acid (COOH) moieties through carboxylation reaction. The significant increase for the amount of carboxyl group on the basal plane of GO will introduce more PPy and improve its dispersion within the composite during electrochemical polymerization, as illustrated in Fig. 1.

FT-IR spectra of GO, GO–COOH, PPy, PPy/GO, and PPy/GO–COOH are presented in Fig. 3a. In the spectrum of GO, peaks at 1729 cm and 1620 cm^{-1} are due to C=O stretching and aromatic C=C stretching vibration or absorbed water [41], respectively. Peaks at 1398 and 1227 cm^{-1} are assigned to O–H deformation and C–OH stretching vibrations [42]. Peak at 1060 cm^{-1} is related to C–O stretching of alkoxy group, and the vibration at 852 cm^{-1} is attributed to epoxide group (C–O–C) [43]. It can be seen that GO–COOH presents the same characteristic absorption peaks as GO, manifesting that they contain the same functional groups. The difference is that the C=O

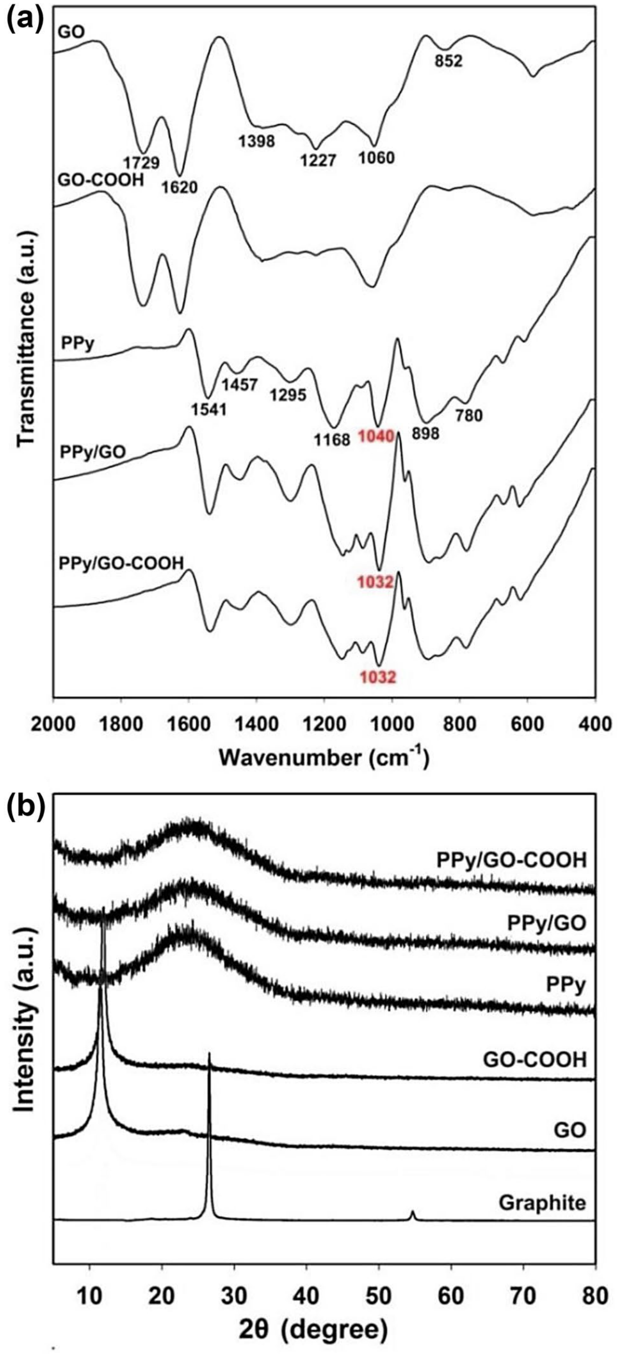

Fig. 3 **a** FT-IR spectra of GO, GO–COOH, PPy, PPy/GO, and PPy/GO–COOH; **b** XRD patterns of graphite, GO, GO–COOH, PPy, PPy/GO, and PPy/GO–COOH

stretching of carboxyl group at 1729 cm^{-1} for GO–COOH is strengthened relative to that of GO. Meanwhile, peaks at 1227 and 852 cm^{-1}, respectively, which originate from C–OH and C–O–C group, are weakened. These are the evidence that hydroxyl (–OH) and epoxide (C–O–C) in GO are partially transformed into carboxyl group (–COOH) through carboxylation reaction, which agrees well with the results of XPS.

For PPy spectrum, main characteristic bands are as follows [44, 45]: C=C ring vibrations at 1541 cm^{-1}, C–C symmetric stretching at 1457 cm^{-1}, C–H (in-plane) stretching at 1295 cm^{-1}, C–N stretching at 1168 cm^{-1}, C–H in-plane deformation of PPy ring at 1040 cm^{-1}, and N–H (wagging) and N–H (out of plane) vibrations at 898 and 780 cm^{-1}, respectively. For PPy/GO and PPy/GO–COOH composites, anionic GO and GO–COOH act as charge balancing dopant during the electropolymerization of PPy. It can be seen that the characteristic peaks of PPy appear in the PPy/GO and PPy/GO–COOH spectra, suggesting the presence of PPy in both of composites. Nevertheless, using the PPy spectrum as a reference, the absorption band situated at 1040 cm^{-1} due to C–H in-plane vibration has downshifted to 1032 cm^{-1} for the two types of composites. This redshift indicates the change in chemical environment of PPy during the composite formation, being related to π-π interactions and hydrogen bonding between the GO or GO–COOH layers and aromatic PPy rings [46]. Additionally, the unobvious bands detected for GO and GO–COOH in the composites is probably because they are too weak, or overlapped with those of PPy coating.

GO, GO–COOH, PPy, PPy/GO, and PPy/GO–COOH composites were further characterized by XRD (Fig. 3b). The pristine graphite shows an intense sharp peak at 2θ = 26.6°, corresponding to an interlayer distance (d-spacing) of 0.335 nm based on the Bragg equation. GO and GO–COOH have sharp peaks at 2θ = 11.4° and 11.8°, respectively, which correspond to d-spacings of 0.78 and 0.75 nm, suggesting that GO treated by carboxylation slightly decreases the d-spacing of nanosheets. Compared to graphite, the increased d-spacing for GO and GO–COOH can be ascribed to the introduction of oxygenated functional groups and intercalated water molecules between layers [47]. Pure PPy shows a broad diffraction peak at 2θ = 24.6°, indicative of amorphous structure, which is close to the distance of interplanar aromatic rings [48, 49]. Both PPy/GO and PPy/GO–COOH composites exhibit almost the same broad diffraction peaks as pure PPy, which are attributed to the diffraction of PPy. The peak ascribed to GO within the composites disappears, probably associated with complete coating of PPy between the layered GO or GO–COOH, which increases their d-spacing [29].

The electrochemical properties of electrode materials are closely related to their surface morphology. Figure 4a shows the SEM images of PPy, PPy/GO, and PPy/GO–COOH. It can be observed that PPy consists of aggregated grains, showing a compact and dense morphology. This is unfavorable to the access of electrolyte, consequently resulting in unsatisfied capacitive properties. However, after GO is introduced into the PPy matrix, PPy/GO exhibits a distinctly different microstructure. Curly sheet-like morphology of GO is

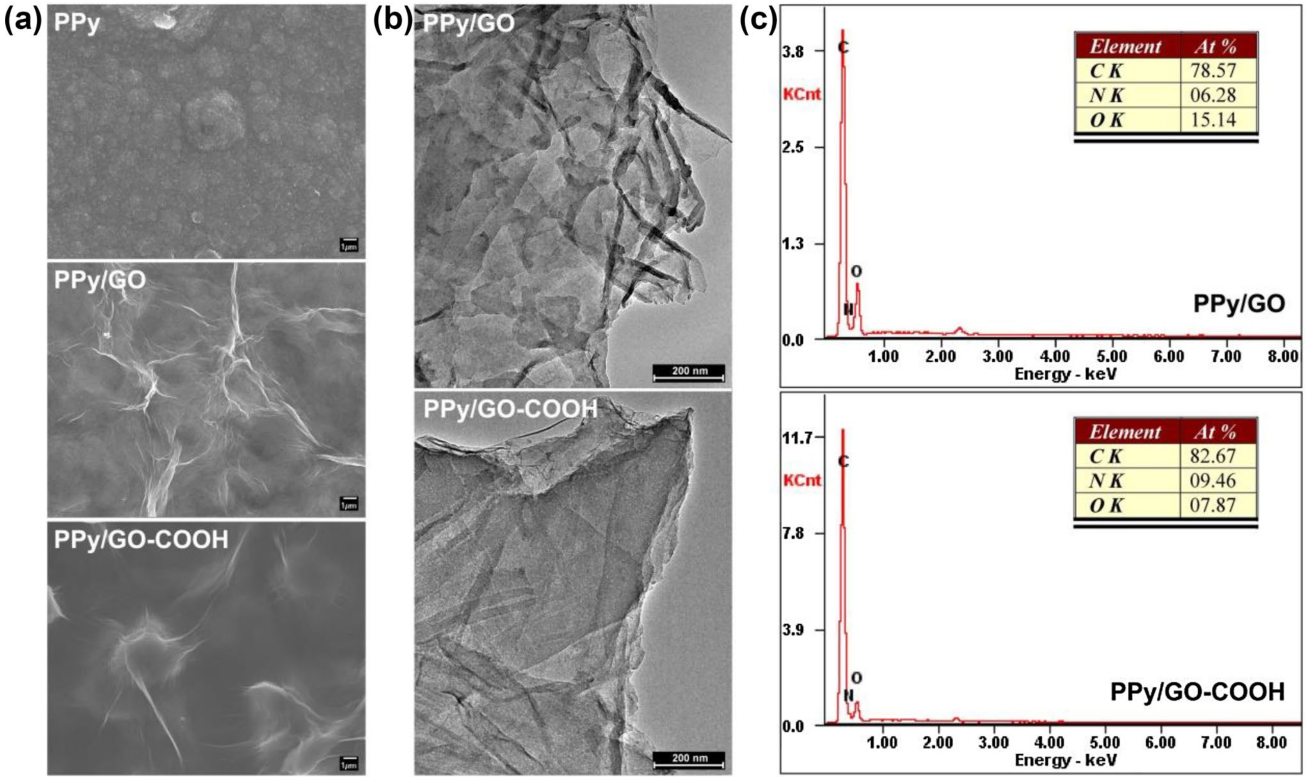

Fig. 4 **a** SEM images of PPy, PPy/GO, and PPy/GO–COOH composites; **b** TEM images and **c** EDS patterns of PPy/GO and PPy/GO–COOH composites

observed clearly and two-dimensional GO nanosheets interconnect with each other. This indicates that GO nanosheets significantly improve the dispersion of PPy, because PPy as coating covers on the GO sheets with large surface area. Such favourable loose microstructures shorten the diffusion path of electrolyte, enabling electrolyte to contact easily with more PPy, which facilitates the utilization of more PPy for electrochemical energy storage. Likewise, it is observed from PPy/GO–COOH image that GO–COOH sheets as the substrate load PPy coating. However, the curly sheet-like morphology becomes not too obvious with respect to that of PPy/GO. As shown in our experiment design (see Fig. 1), it is caused by larger amount of PPy coatings on GO–COOH sheets, covering their curly morphology.

TEM images in Fig. 4b reveal more morphological details for the as-prepared composites. It is obvious that PPy/GO composite has more obvious dark area by curly sheet-like morphology than PPy/GO–COOH. Moreover, a careful inspection of the edge of the two types of composites suggests that significantly more PPy is present for PPy/GO–COOH composite. TEM characterizations are in line with SEM results. EDS tests were performed to determinate elementary composition of the composites. As shown in Fig. 4c, PPy/GO–COOH has an increased atom ratio of C:O due to the introduction of more PPy, in particular, atom ratio of N originating from PPy increases from 6.28% for PPy/GO to 9.46% for PPy/GO–COOH, further indicating that more PPy is introduced into latter composite.

3.2 Electrochemical properties

Figure 5a presents the CV curves at scan rate of 10 mV s^{-1} for PPy, PPy/GO, and PPy/GO–COOH electrodes. PPy electrodes show the shape deviating from rectangle, due to unsatisfactory supercapacitive performance. Compared with PPy electrodes, both PPy/GO and PPy/GO–COOH electrodes have the rectangle-like shape. However, the shape of PPy/GO–COOH electrodes is closer to rectangle relative to that of PPy/GO electrodes. Additionally, PPy/GO–COOH electrodes also show superior rate capability (Fig. 5b). The current density persistently increases at higher scan rate, and the rectangle-like CV curves show almost symmetric I-E responses up to 100 mV s^{-1}.

Note that areal specific capacitance is a better performance indicator when supercapacitors are used for small scale electronics and energy storage of stationary devices [50–52]. For this reason, our research will focus on areal specific capacitance, which can be calculated from the CV curves by the following equation:

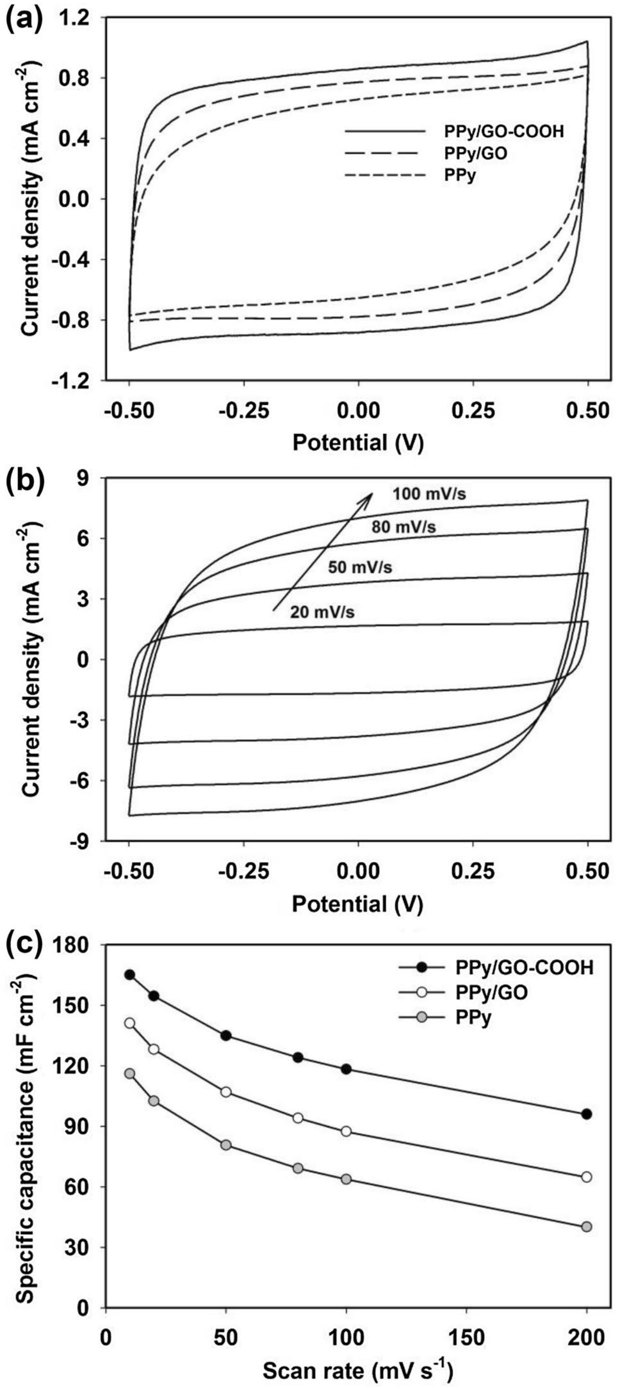

Fig. 5 **a** CV curves at the scan rate of 10 mV s^{-1} for PPy, PPy/GO, and PPy/GO–COOH composite electrodes. **b** CV curves at the scan rate range from 20 to 100 mV s^{-1} for PPy/GO–COOH composite electrode. **c** Relationship of areal specific capacitance with CV scan rate for PPy, PPy/GO, and PPy/GO–COOH composite electrodes

$$C_S = \left(\int IdV \right) / (S \times \Delta V \times v) \tag{1}$$

where C_S represents the areal specific capacitance of electrode in F cm^{-2}; $\int I\,dV$ the integrated area of the CV curve; S the geometric surface area of electrode in cm^2; ΔV the scanning potential window in V; and v the scan rate in V s^{-1}. Figure 5c shows that PPy/GO–COOH electrodes have the largest specific capacitance at all scan rates, while PPy electrodes exhibit the lowest. Thereinto, the PPy/GO–COOH electrodes deliver a specific capacitance of 165.5 mF cm^{-2} at 10 mV s^{-1}, which is 17.6% higher than 140.7 mF cm^{-2} for PPy/GO electrodes, as well as 42.5% higher than 116.1 mF cm^{-2} for PPy electrodes. Compared with PPy, the enhanced capacitive performance for PPy/GO and PPy/GO–COOH can be attributed to the fact that the introduced GO and GO–COOH nanosheets increase the specific surface area of electrodes and hence improve the dispersion of PPy, making more PPy to be utilized for charge storage. Meanwhile, the hydrophilic GO and GO–COOH nanosheets add the wettability of composite electrodes, enabling electrolyte to access easily. Compared with PPy/GO, the promoted capacitive performance for PPy/GO–COOH is related to more polymerized PPy, which is caused by more carboxyl group in GO–COOH as counter anion.

GCD measurements were made to further compare the supercapacitive performances of two types of PPy composites. Figure 6a presents the GCD curves at 0.5 mA cm^{-2} of PPy/GO and PPy/GO–COOH electrodes. Both exhibit triangle-shaped curves, but PPy/GO–COOH electrodes have longer discharge time. Moreover, columbic efficiency (η) of electrodes can be obtained by calculating the ratio of discharge time (t_d) to charge time (t_c). At the current density of 0.5 mA cm^{-2}, the η of PPy/GO–COOH electrodes is 95.2%, which is higher than 93.5% of PPy/GO electrodes. Further observation from Fig. 6b manifests that PPy/GO–COOH electrodes have obviously lower IR drop relative to PPy/GO, which indicates that the supercapacitor cell assembled with PPy/GO–COOH electrodes has a smaller internal resistance. This is of importance for energy-storing devices, since it will save energy through reducing the production of unwanted heat during the processes of charging/discharging [53]. Specific capacitance of electrodes can be obtained according to GCD curves from the Eq. (2):

$$C_S = (2 \times I \times t)/(S \times \Delta V) \tag{2}$$

here C_S (F cm^{-2}) is the areal specific capacitance, I (A) the discharge current, t (s) the discharge time, S (cm^{-2}) the geometric surface area of electrode, and ΔV (V) the scanning potential window. It can be seen from Fig. 6c that the PPy/GO–COOH electrodes have higher specific capacitance at various current densities ranging from 0.5 to 10 mA cm^{-2}, in line with the CV results. PPy/GO electrodes achieve a C_S of 146.3 mF cm^{-2} at 0.5 mA cm^{-2}, whereas the C_S of PPy/GO–COOH electrodes rises to as high as 170.9 mF cm^{-2} at 0.5 mA cm^{-2}. The latter value is to be compared with those of recently reported CP based electrode materials: polyoxometalate (POM)-doped PPy nanopillar (77.0 mF cm^{-2}

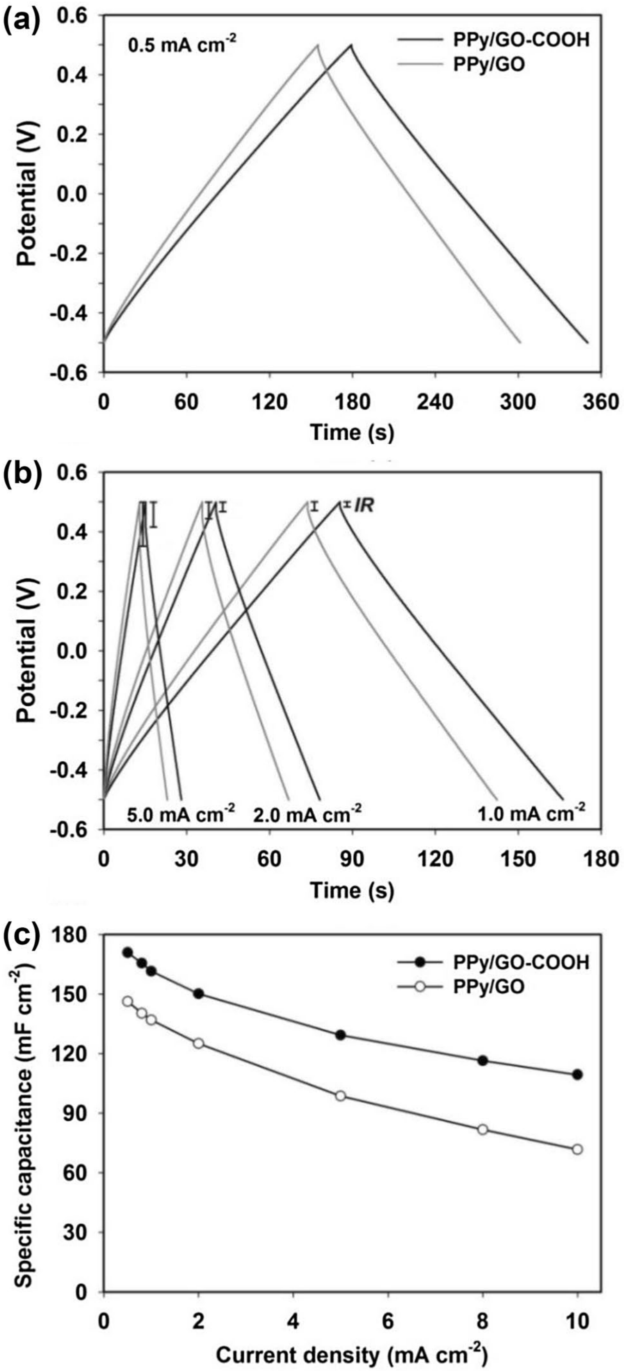

Fig. 6 GCD curves at current density of **a** 0.5 and **b** 1.0, 2.0, and 5.0 mA cm^{-2}. Shown in **c** are plots of specific capacitance versus GCD current density for PPy/GO and PPy/GO–COOH composite electrodes

at 1 mA cm^{-2}) [54], 3D porous graphene/PANI composite (67.2 mF cm^{-2} at 0.05 mA cm^{-2}) [55], H-TiO$_2$/Prussian blue/PEDOT (40.0 mF cm^{-2} at 0.45 mA cm^{-2}) [56], rGO/PEDOT (43.75 mF cm^{-2} at 0.2 mA cm^{-2}) [57], and graphite oxide/PANI composite (6.3 mF cm^{-2} at 0.16 mA cm^{-2}) [51].

Furthermore, with the increase of current density, specific capacitance of PPy/GO–COOH electrodes shows a trend of relatively smooth decline relative to that of PPy/GO electrodes. When the current density is increased by as much as 20 times, PPy/GO–COOH electrodes retain 64.0% of initial capacitance (109.4 mF cm^{-2} at 10 mA cm^{-2}), while PPy/GO electrodes only maintain 49.0% (71.7 mF cm^{-2} at 10 mA cm^{-2}), suggesting that PPy/GO–COOH electrodes have superior rate capability, which is related with the relatively dispersed PPy.

Figure 7a illustrates the Nyquist plots of PPy/GO and PPy/GO–COOH electrodes. Capacitive character is observed for both types of electrodes, because both display a vertical trend for impedance plots at low frequencies. Nevertheless, in low frequency region, the straight line of PPy/GO–COOH electrodes leans more towards the imaginary axis, indicating that they have better capacitive behavior [58]. Another important piece of information that can be obtained at high frequency is the equivalent series resistance (ESR), which is determined by the intercept at the x-axis in EIS plot. It is related to the electrolyte solution resistance, intrinsic resistance of active materials, and interfacial contact resistance between active materials and current collectors [59]. As shown in the inset of Fig. 7a, compared to PPy/GO electrodes, the PPy/GO–COOH electrodes have smaller ESR, a key specification to electrochemical energy-storing devices. In line with CV and GCD results, EIS tests further demonstrate that PPy/GO–COOH electrodes have superior capacitive behaviors. As described in morphology characterizations, compared with PPy/GO composite, the enhanced electrochemical capacitive properties for PPy/GO–COOH composite are because more PPy with superior pseudocapacitive properties is introduced into composite, that is, all-round carboxyl-covered nanosheets with edged and basal oxygen-containing sites for GO–COOH provide more active sites for PPy heterogeneous nucleation, which also facilitates the formation of a stable, uniform, orderly composite structure.

3.3 Stability and ragone plot

Cycling stability is a significant performance index to evaluate electrode materials for supercapacitors. Figure 7b exhibits the variation of capacitance retention of PPy/GO and PPy/GO–COOH electrodes suffered from 5000 CV cycles at the scan rate of 80 mV s^{-1}. The cycling measurements result in an increase in specific capacitance for the two types of electrodes at the beginning. After 1000 cycles, their specific capacitances start to decline. This is because cycling tests induce more electroactive surface area with the surface gradual wetting, due to the hydrophilic nature of GO and GO–COOH nanosheets [60]. After 5000 cycles, PPy/GO and PPy/GO–COOH electrodes retain 93.7 and

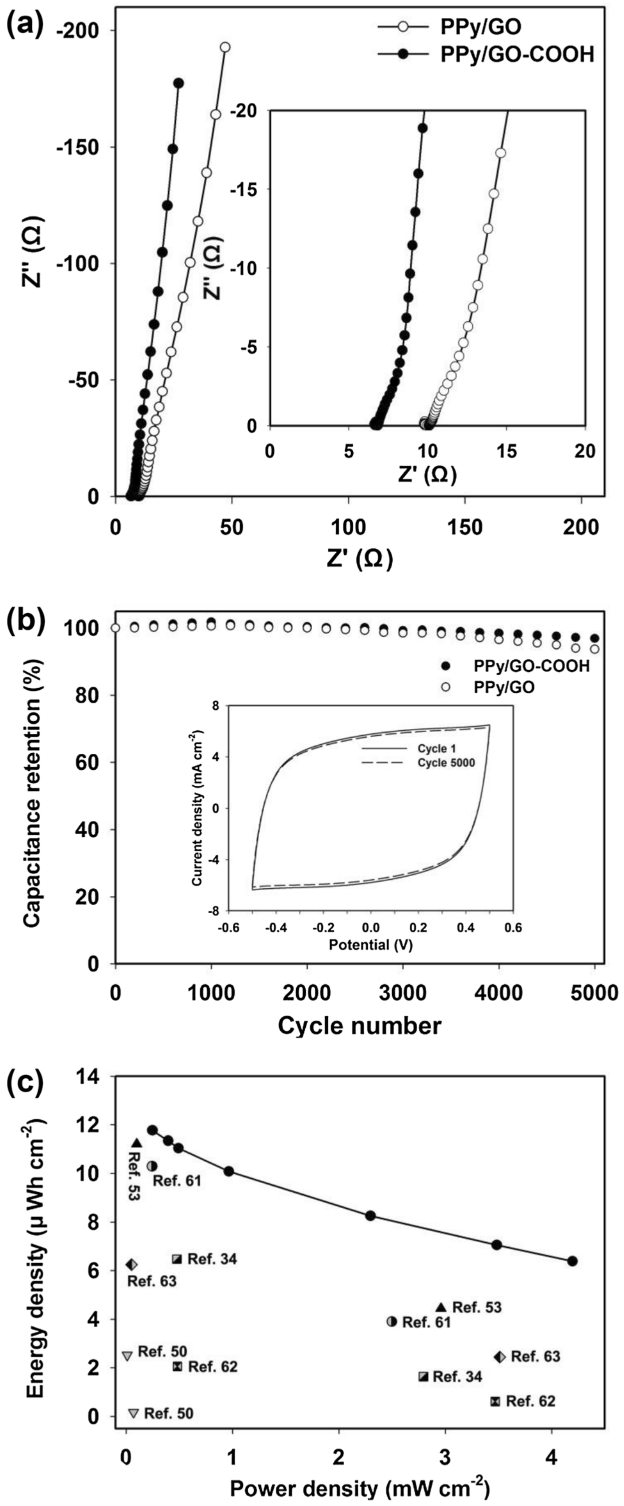

Fig. 7 **a** Nyquist plots of PPy/GO and PPy/GO–COOH composite electrodes. The insert is the EIS plots at high frequencies. **b** Plots of capacitance retention as a function of cycle number for PPy/GO and PPy/GO–COOH composite electrodes. The inset presents CV curves at 80 mV s^{-1} of PPy/GO–COOH at cycle 1 and cycle 5000. **c** Ragone plot of supercapacitor consisting of symmetric PPy/GO–COOH composite electrodes, as compared with data from previous supercapacitors composed of CP based composite electrodes

96.9% of the initial capacitance, respectively, indicative of their superior cycling stability. The higher stability for PPy/GO–COOH electrodes is possibly associated with the introduction of more relatively dispersed PPy, in which carboxyl groups distributed on the basal plane and edges of GO–COOH nanosheets are utilized to combine with PPy. In contrast, only carboxyl groups restricted at the edges can be employed to combine with PPy for GO nanosheets. Besides, better hydrophilicity for GO–COOH contributes to improving the wettability of electrode materials to electrolyte during cycling.

Energy density and power density of a supercapacitor are two key metrics to evaluate its performances. Areal specific energy density and power density of the tested supercapacitor cell consisting of two pieces of identical PPy/GO–COOH electrodes is calculated from Eqs. (3) and (4) [34, 51], respectively:

$$E = \frac{\frac{1}{2}C_S \Delta V^2}{3600} \tag{3}$$

$$P = \frac{3600E}{t} \tag{4}$$

where E is the areal specific energy density in Wh cm^{-2}; P the areal specific power density in W cm^{-2}; C_S the areal specific capacitance of supercapacitor in F cm^{-2}; ΔV is the potential window subtracting IR drop in V; t the discharge time in s; and 3600 is for unit conversion between second and hour. Figure 7c presents the Ragone plot of the tested supercapacitor cell composed of PPy/GO–COOH electrodes. It achieves the highest power density of 4.2 mW cm^{-2} and the maximum energy density of 11.8 μWh cm^{-2}, which also shows higher energy density and power density than other recently reported CP based supercapacitors such as PPy–GO [34], PANI/graphite oxide [50], PPy/CNTs [46], PPy/GO/CNTs [61], PPy-carbon paper [62], and PEDOT/SDS-GO [63]. This makes PPy/GO–COOH composite competitive electrode materials for high-performance supercapacitor applications.

4 Conclusions

To adequately utilize the oxygenated groups on the basal plane of GO to combine with PPy, GO has suffered from a treatment of carboxylation in this work. Through the treatment, hydroxyl and epoxide on the basal plane of GO are partially converted into carboxylic acid moieties. PPy/GO and PPy/GO–COOH composites are prepared by in-situ electrochemical polymerization. Both of them show superior electrochemical behaviors with respect to PPy. More importantly, the obtained PPy/GO–COOH composites have a different morphology and obviously enhanced supercapacitive performances relative to PPy/GO composites. This is ascribed to the fact that GO–COOH provides more active sites for the dispersion and polymerization of PPy due to its all-round carboxyl-covered nanosheets with edged and basal oxygen-containing sites. The PPy/GO–COOH composite electrodes exhibit a high areal specific capacitance of 170.9 mF cm^{-2} at 0.5 mA cm^{-2}, superior rate capability, as well as cycling stability (retaining 96.9% of initial capacitance for 5000 cycles), indicating the potential applications in supercapacitors. This work is anticipated to stimulate further research interest for GO–COOH based composite electrodes in electrochemical energy storage applications.

Acknowledgements This work was supported by the National Natural Science Foundation of China (21601113 and 21573138), the China Postdoctoral Science Foundation (2015M571283), the Natural Science Foundation of Shanxi Province (2015021079), the Scientific and Technological Innovation Programs of Higher Education Institutions in Shanxi (2017112), and the Sanjin Scholar Distinguished Professors Program.

References

1. E. Mourad, L. Coustan, P. Lannelongue, D. Zigah, A. Mehdi, A. Vioux, S.A. Freunberger, F. Favier, O. Fontaine, Nat. Mater. **16**, 446–453 (2017)
2. C.J. Chen, Y. Zhang, Y.J. Li, J.Q. Dai, J.W. Song, Y.G. Yao, Y.H. Gong, I. Kierzewski, J. Xie, L.B. Hu, Energy Environ. Sci. **10**, 538–545 (2017)
3. C. Choi, J.M. Lee, S.H. Kim, S.J. Kim, J.T. Di, R.H. Baughman, Nano Lett. **16**, 7677–7684 (2016)
4. J.W. Yuan, S.H. Tang, Z.T. Zhu, X.L. Qin, R.J. Qu, Y.X. Deng, L.S. Wu, J. Li, G.M. Haarberg, J. Mater. Sci. Mater. Electron. **28**, 18022–18030 (2017)
5. T. Liu, C.J. Jiang, W. You, J.G. Yu, J. Mater. Chem. A. **5**, 8635–8643 (2017)
6. M.A. Maier, R.S. Babu, D.M. Sampaio, A.L.F. de Barros, J. Mater. Sci. Mater. Electron. **28**, 17405–17413 (2017)
7. Y. Yang, Q.Y. Huang, L.Y. Niu, D.R. Wang, C. Yan, Y.Y. She, Z.J. Zheng, Adv. Mater. **29**, 1606679 (2017)
8. Y. Huang, H.F. Li, Z.F. Wang, M.S. Zhu, Z.X. Pei, Q. Xue, Y. Huang, C.Y. Zhi, Nano Energy. **22**, 422–438 (2016)
9. X. Gao, H.Y. Yue, E.J. Guo, L.H. Yao, X.Y. Lin, B. Wang, E.H. Guan, D. Bychanok, J. Mater. Sci. Mater. Electron. **28**, 17939–17947 (2017)
10. Y. Wang, W.H. Lai, N. Wang, Z. Jiang, X.Y. Wang, P.C. Zou, Z.Y. Lin, H.J. Fan, F.Y. Kang, C.P. Wong, C. Yang, Energy Environ. Sci. **10**, 941–949 (2017)
11. X.L. Su, L. Fu, M.Y. Cheng, J.H. Yang, X.X. Guan, X.C. Zheng, Appl. Surf. Sci. **426**, 924–932 (2017)
12. L.Y. Jiang, Y.W. Sui, J.Q. Qi, Y. Chang, Y.Z. He, Q.K. Meng, F.X. Wei, Z. Sun, Y.X. Jin, Appl. Surf. Sci. **426**, 148–159 (2017)
13. S.J. Im, Y.R. Park, S. Park, H.J. Kim, J.H. Doh, K. Kwon, W.G. Hong, B. Kim, W.S. Yang, T.Y. Kim, Y.J. Hong, Appl. Surf. Sci. **412**, 160–169 (2017)
14. T. Liu, C.J. Jiang, B. Cheng, W. You, J.G. Yu, J. Power Sources. **359**, 371–378 (2017)
15. Z.S. Liu, D.H. Li, Z.S. Li, Z.H. Liu, Z.Y. Zhang, Appl. Surf. Sci. **422**, 339–347 (2017)
16. M. Devi, A. Kumar, J. Appl. Polym. Sci. **135**, 45883 (2018)
17. J. Zhu, L.R. Kong, X.P. Shen, Q.R. Chen, Z.Y. Ji, J.H. Wang, K.Q. Xu, G.X. Zhu, Appl. Surf. Sci. **428**, 348–355 (2018)
18. D.P. Dubal, N.R. Chodankar, Z. Caban-Huertas, F. Wolfart, M. Vidotti, R. Holze, C.D. Lokhande, P. Gomez-Romero, J. Power Sources. **308**, 158–165 (2016)
19. Y. Huang, M.S. Zhu, Z.X. Pei, Y. Huang, H.Y. Geng, C.Y. Zhi, ACS Appl. Mater. Interfaces. **8**, 2435–2440 (2016)
20. G.A. Snook, P. Kao, A.S. Best, J. Power Sources. **196**, 1–12 (2011)
21. J.S. Lee, D.H. Shin, W. Kim, J. Jang, J. Mater. Chem. A. **4**, 6603–6609 (2016)
22. X.Y. Fan, X.L. Wang, G. Li, A.P. Yu, Z.W. Chen, J. Power Sources. **326**, 357–364 (2016)
23. L.Y. Yuan, C.Y. Wan, X.R. Ye, F.H. Wu, Electrochim. Acta. **213**, 115–123 (2016)
24. X. Jian, H.M. Yang, J.G. Li, E.H. Zhang, L.L. Cao, Z.H. Liang, Electrochim. Acta. **228**, 483–493 (2017)
25. A. Afzal, F.A. Abuilaiwi, A. Habib, M. Awais, S.B. Waje, M.A. Atieh, J. Power Sources. **352**, 174–186 (2017)
26. F.M. Guo, R.Q. Xu, X. Cui, L. Zhang, K.L. Wang, Y.W. Yao, J.Q. Wei, J. Mater. Chem. A. **4**, 9311–9318 (2016)
27. S. Lehtimaki, M. Suominen, P. Damlin, S. Tuukkanen, C. Kvarnstrom, D. Lupo, ACS Appl. Mater. Interfaces. **7**, 22137–22147 (2015)
28. J.Y. Cao, Y.M. Wang, J.C. Chen, X.H. Li, F.C. Walsh, J.H. Ouyang, D.C. Jia, Y. Zhou, J. Mater. Chem. A. **3**, 14445–14457 (2015)
29. C.Z. Zhu, J.F. Zhai, D. Wen, S.J. Dong, J. Mater. Chem. **22**, 6300–6306 (2012)
30. L.Q. Fan, G.J. Liu, J.H. Wu, L. Liu, J.M. Lin, Y.L. Wei, Electrochim. Acta. **137**, 26–33 (2014)
31. I.M.D. Salas, Y.N. Sudhakar, M. Selvakumar, Appl. Surf. Sci. **296**, 195–203 (2014)
32. J. Li, H.Q. Xie, Y. Li, J. Power Sources. **241**, 388–395 (2013)
33. K. Qi, Y.B. Qiu, X.P. Guo, Electrochim. Acta. **137**, 685–692 (2014)
34. H.H. Zhou, G.Y. Han, Y.M. Xiao, Y.Z. Chang, H.J. Zhai, J. Power Sources. **263**, 259–267 (2014)
35. S. Park, R.S. Ruoff, Nat. Nanotechnol. **4**, 217–224 (2009)
36. W.S. Hummers, R.E. Offeman, W.S. Hummers, R.E. Offeman, J. Am. Chem. Soc. **80**, 1339 (1958)
37. Y.X. Xu, H. Bai, G.W. Lu, C. Li, G.Q. Shi, J. Am. Chem. Soc. **130**, 5856–5857 (2008)
38. X.M. Sun, Z. Liu, K. Welsher, J.T. Robinson, A. Goodwin, S. Zaric, H.J. Dai, Nano Res. **1**, 203–212 (2008)
39. K. Zhang, N. Heo, X. Shi, J.H. Park, J. Phys. Chem. C. **117**, 24023–24032 (2013)
40. R. Imani, S.H. Emami, S. Faghihi, J. Nanopart. Res. **17**, 88 (2015)
41. M. Bagherzadeh, Z.S. Ghahfarokhi, E.G. Yazdi, RSC Adv. **6**, 22007–22015 (2016)
42. C. Bora, S.K. Dolui, Polymer. **53**, 923–932 (2012)
43. N. Pan, D.B. Guan, Y.T. Yang, Z.L. Huang, R.B. Wang, Y.D. Jin, C.Q. Xia, Chem. Eng. J. **236**, 471–479 (2014)
44. C.X. Wang, G.J. Shao, Z.P. Ma, S. Liu, W. Song, J.J. Song, Electrochim. Acta. **130**, 679–688 (2014)
45. Y. Shi, L.J. Pan, B.R. Liu, Y.Q. Wang, Y. Cui, Z.A. Bao, G.H. Yu, J. Mater. Chem. A. **2**, 6086–6091 (2014)
46. A. Singh, A. Chandra, J. Appl. Electrochem. **43**, 773–782 (2013)
47. H.L. Guo, X.F. Wang, Q.Y. Qian, F.B. Wang, X.H. Xia, ACS Nano. **3**, 2653–2659 (2009)
48. Y. Liu, H.H. Wang, J. Zhou, L.Y. Bian, E.W. Zhu, J.F. Hai, J. Tang, W.H. Tang, Electrochim. Acta. **112**, 44–52 (2013)
49. H. Zhou, T. Ni, X.T. Qing, X.X. Yue, G. Li, Y. Lu, RSC Adv. **4**, 4134–4139 (2014)

50. H.G. Wei, J.H. Zhu, S.J. Wu, S.Y. Wei, Z.H. Guo, Polymer. **54**, 1820–1831 (2013)
51. J.F. Sun, Y. Huang, C.X. Fu, Y. Huang, M.S. Zhu, X.M. Tao, C.Y. Zhi, H. Hu, J. Mater. Chem. A. **4**, 14877–14883 (2016)
52. Z.S. Wu, K. Parvez, S. Li, S. Yang, Z.Y. Liu, S.H. Liu, X.L. Feng, K. Muellen, Adv. Mater. **27**, 4054–4061 (2015)
53. H.H. Zhou, G.Y. Han, Y.M. Xiao, Y.Z. Chang, H.J. Zhai, Synth. Met. **209**, 405–411 (2015)
54. M. Yang, S.B. Hong, J.H. Yoon, D.S. Kim, S.W. Jeong, D.E. Yoo, T.J. Lee, K.G. Lee, S.J. Lee, B.G. Choi, ACS Appl. Mater. Interfaces. **8**, 22220–22226 (2016)
55. Q.Q. Zhou, Y.R. Li, L. Huang, C. Li, G.Q. Shi, J. Mater. Chem. A. **2**, 17489–17494 (2014)
56. M. Szkoda, K. Trzcinski, J. Rysz, M. Gazda, K. Siuzdak, A. Lisowska-Oleksiak, Solid State Ionics. **302**, 197–201 (2017)
57. X.L. Mao, W.Y. Yang, X. He, Y. Chen, Y.T. Zhao, Y.J. Zhou, Y.J. Yang, J.H. Xu, Mater. Sci. Eng. B. **216**, 16–22 (2017)
58. C. Peng, J. Jin, G.Z. Chen, Electrochim. Acta. **53**, 525–537 (2007)
59. Y.R. Wang, H.G. Wei, J.M. Wang, J.R. Liu, J. Guo, X. Zhang, B.L. Weeks, T.D. Shen, S.Y. Wei, Z.H. Guo, J. Mater. Chem. A. **3**, 20778–20790 (2015)
60. Y.F. Xu, I. Hennig, D. Freyberg, A.J. Strudwick, M.G. Schwab, T. Weitz, K.C.P. Cha, J. Power Sources. **248**, 483–488 (2014)
61. H.H. Zhou, G.Y. Han, Electrochim. Acta. **192**, 448–455 (2016)
62. H.G. Wei, Y.R. Wang, J. Guo, X.R. Yan, R. O'Connor, X. Zhang, N.Z. Shen, B.L. Weeks, X.H. Huang, S.Y. Wei, Z.H. Guo, Chemelectrochem. **2**, 119–126 (2015)
63. H.H. Zhou, G.Y. Han, D.Y. Fu, Y.Z. Chang, Y.M. Xiao, H.J. Zhai, J. Power Sources. **272**, 203–210 (2014)